FCC feasibility studies: Impact of tracker- and calorimeter-detector performance on jet flavor identification and Higgs physics analyses, and study of Higgs-to-invisible performance with CLD full simulation

H. Abidi[1] K. A. Assamagan[1] D. Boye[1] L. Brost[1] V. Cavaliere[1] A. E. Connelly[1] D. Garcia[2] G. Iakovidis[1] A. Li[1] M.-A. Pleier[1], A. Sciandra[1*], M. Selvaggi[2] S. Snyder[1] R. Szafron[1] A. Tishelman-Charny[1] I. Veliscek[1]

[1]Physics Department, Brookhaven National Laboratory, Upton NY; United States of America.

[2]CERN, Geneva; Switzerland

ABSTRACT

The extensive and ambitious physics program planned at the FCC-ee imposes strict constraints on the detector performance. This works aims at studying the impact of different detector choices on the identification of the jet flavor and how this affects high-profile analysis like Higgs-boson couplings and searches for invisible decays of the Higgs-boson. Furthermore, a first study of the Higgs-to-invisible performance with the CLD-detector full simulation is performed.

Keywords: FCC-ee – feasibility study – flavor tagging – Higgs physics – detector performance – CLD full simulation

1. INTRODUCTION

The Future Circular Collider for electrons and positrons (FCC-ee) project [1] aims to explore particle physics frontiers with unprecedented precision.

Several detectors have been proposed [2–5], each with specific sub-detector configurations and geometries. This study examines how different detector choices impact high-profile analyses, particularly focusing on tracker configurations and their effects on jet flavor identification (jet-tagging). We evaluate how these choices influence Higgs boson coupling measurements and Higgs self-coupling analysis. Additionally, we assess various calorimeter designs for detecting invisible Higgs boson decays.

Accurate jet flavor identification is crucial for measuring Higgs boson couplings. These algorithms distinguish between fundamental particles produced in high-energy collisions, enabling precise Standard Model measurements and detection of new physics phenomena. They are essential for the FCC-ee physics program's core objectives: precision Higgs boson studies, top-quark measurements, and searches for physics beyond the Standard Model. These algorithms guide detector optimization and drive technological advancement.

We developed an algorithm [6] for reconstructing track parameters and covariance matrices of charged particles for arbitrary tracking geometries, alongside a graph neural network-based jet flavor identification system. Using the FCC-ee IDEA detector prototype, we evaluated various configurations: adding a fourth innermost pixel detector layer and incorporating particle-identification data through cluster-counting (dN/dx) and time-of-flight measurements.

At 240 GeV center-of-mass energy and 5 ab $\times\ 10^{-1}$ integrated luminosity, the FCC-ee will produce millions of Higgs bosons primarily through Higgs-strahlung (ZH). The clean e^+e^- collision environment enables direct measurement of Higgs branching fractions, contrasting with the ratio measurements at hadron colliders. Advanced flavor tagging techniques may enable the first observation of Higgs-charm quark coupling.

Regarding invisible Higgs decays, Standard Model coupling measurements suggest up to 30% of the total width could involve beyond Standard Model decays. While the Standard Model predicts $H \to ZZ \to 4\nu$ with $O(10^{-3})$ branching fraction, this could increase if Higgs decays into weakly interacting massive particles (WIMPs), potentially explaining dark matter. Operating at $\sqrt{s} \sim 240\,\text{GeV}$ and $365\,\text{GeV}$, the FCC-ee could detect branching ratios below one per mille. Current studies examine the ZH process (Z $\to f\bar{f}$, H $\to$ invisible) using full CLD [4] simulation.

Section 2 details event generation and simulation across detector configurations. Section 2.2 presents extended flavor-tagging performance studies, while Section 4 discusses implications for Higgs coupling measurements. Sections 2.3 and 5 examine calorimeter variations' effects on Higgs-to-invisible searches.

2. GENERATION, SIMULATION AND DETECTOR VARIATIONS

Higgsstrahlung events at a FCC-ee-like Higgs factory ($e^+e^- \to ZH$) have been generated through the WHIZARD [7] generator at a center-of-mass energy $\sqrt{s} = 240$ GeV and simulated through Delphes [8], see Section 2.1. Five different Higgs-boson decay modes corresponding to each jet flavor category - bottom (b), charm (c), strange (s), gluon (g) and up/down ($q = u, d$) - have been combined with the Z-boson decay to a pair of neutrinos (ν), so that there is no ambiguity in the assignment of hadronic products to the Higgs-boson decay. A total of one million $e^+e^- \to Z(\to \nu\nu)H$ events has been produced, equally divided upon the five different families of flavors, in order to conduct the flavor-tagging performance studies discussed in the following. **It has to be noted that the jet-flavour tagging performance studies were extended to run trainings on a sample of ten million jets per flavour for the baseline IDEA detector and the most important detector variations. Relative variations in the expected tagger performance prove to be mostly invariant under extensions of the training input datasets and, thus, with respect to absolute algorithm performance.**

In addition to the $e^+e^- \to Z(\to \nu\nu)H$ events the fully hadronic analysis uses the $e^+e^- \to Z(\to jj)H(\to jj)$ samples split by the final state. The Z decays to b, c, s and q and the H decays to b, c, s, gluon g, tau τ, Z, $Z\gamma$ and W are considered. Table 1 shows the process considered and their split in event generation. The main backgrounds, WW, ZZ and Zqq, are generated with Pythia8. The samples and statistics used in the ZH fully hadronic analysis are summarized in Table 1.

The Higgs to invisible analysis uses $e^+e^- \to ZH$ events with Higgs to invisible decays as the signal. Section 5 lists the full simulation samples used in the analysis. Main background are ZZ and ZH generated with Pythia8.

2.1. IDEA detector concept and Delphes setup

The official Delphes fast simulation framework with key additions, such as the TrackCovariance [9], TimeOfFlight [10] and ClusterCounting [11] packages discussed in Ref. [6], is exploited to simulate the detector response. A recent IDEA detector prototype [2, 3] is assumed as the baseline detector configuration.

The IDEA conceptual experiment is based on innovative technologies developed in recent years. It features

Process	Number of events generated
WW	373,375,386
ZZ	56,162,093
Zqq	100,559,248
Z(bb)H($\tau\tau$)	400,000
Z(bb)H(cc)	400,000
Z(bb)H(bb)	100,000
Z(bb)H(ss)	400,000
Z(bb)H(gg)	400,000
Z(bb)H(WW)	1,000,000
Z(bb)H(Zγ)	1,000,000
Z(bb)H(ZZ)	1,000,000
Z(cc)H(cc)	400,000
Z(cc)H(bb)	200,000
Z(cc)H(ss)	300,000
Z(cc)H(gg)	400,000
Z(cc)H(WW)	1,200,000
Z(cc)H(Zγ)	400,000
Z(cc)H(ZZ)	400,000
Z(cc)H($\tau\tau$)	400,000
Z(ss)H(cc)	300,000
Z(ss)H(bb)	200,000
Z(ss)H(ss)	300,000
Z(ss)H(gg)	400,000
Z(ss)H(WW)	1,200,000
Z(ss)H(Zγ)	300,000
Z(ss)H(ZZ)	600,000
Z(ss)H($\tau\tau$)	400,000
Z(qq)H(cc)	200,000
Z(qq)H(bb)	500,000
Z(qq)H(ss)	400,000
Z(qq)H(gg)	400,000
Z(qq)H(WW)	1,100,000
Z(qq)H(Zγ)	393,135
Z(qq)H(ZZ)	1,200,000
Z(qq)H($\tau\tau$)	200,000

Table 1. The samples used in the fully hadronic ZH analysis.

a Silicon Inner Tracker, surrounded by a very light Drift Chamber and by a Silicon wrapper. The Inner detector is immersed in a 2T magnetic field, generated by a very thin superconducting solenoid. A dual readout calorimeter is positioned outside the magnet, and within the return joke of the magnet. A muon tracker, based on μ-Rwell technology, is interleaved with the return joke material. This same technology also provides a layer of pre-shower in front of the calorimeter.

Variations of detector properties with respect to the baseline described in the next sections are performed in both, the inner and the calorimeter detectors, to evaluate their impact on flavour-identification performance and Higgs-boson measurements at the FCC-ee.

2.2. Variations in tracker-detector properties and layout

Jet flavour identification algorithms play a crucial role in deciphering complex event signatures, allowing for precise measurements at the FCC-ee. Enhanced tracking resolution improves accuracy but often requires additional detector material (e.g. more layers of silicon detector), which can reduce the rejection efficiency of unwanted flavors. Characterizing and balancing these benefits and drawbacks is essential to optimize the tracker layouts for future colliders.

For each detector variation, retraining of the jet flavor identification algorithms is necessary in order to achieve a fair and meaningful performance assessment of each point in the detector-configuration space. Fig. 1 shows the Receiver Operating Characteristic (ROC) curves for the baseline detector and a detector variation, both with and without re-training on the sample accounting for such variations. The performance of the algorithm, trained on the sample simulated through a given detector layout, evaluated on a sample simulated through an alternative detector layout may significantly over- or under-estimate the magnitude of the effects involved. For instance, a significant portion of the algorithm performance degradation due to a potential worsening in the detector performance may be recovered by exposing it to the corresponding sample features. Therefore, all of the tagger-performance studies discussed in the following rely on algorithms trained and evaluated on consistent input samples.

2.2.1. Tracker single-point resolution

The nominal single-point resolution achievable by the $25 \times 25\,\mu\text{m}^2$ pitch vertex detector [12] is of $3\,\mu$m, which is assumed for the baseline IDEA detector simulations. Relative variations of ±65% in the single-point resolution, direct byproduct of the hit resolution, show the great importance played by this vertex-detector property in the determination of the jet flavor. As shown in ROC curves in Fig. 2, the rejection of s-jets is significantly sensitive to the single-point resolution. Effects are quite symmetric in the higher c-efficiency range, with factors of $\simeq 2$ improvement or degradation in s-rejection.

On the other hand, asymmetric effects are observed in the rejection of b-jets for c-tagging, indicating that asymptotic momentum resolution may not be so generally relevant at the FCC-ee because of the relative low momenta ($p_{\mathrm{T}} \leq 50$ GeV) of most of the tracks in the jets. As shown in Fig. 2, better tracker resolution does not greatly benefit the rejection of b-jets, fundamental aspect for $H \to cc$ analyses. Similar impacts are observed on rejection of jets originating from other flavors, while tagging c-jets. Significantly smaller effects are observed in b- and s-tagging, where relative effects in rejecting other flavors are within $10 - 20\%$.

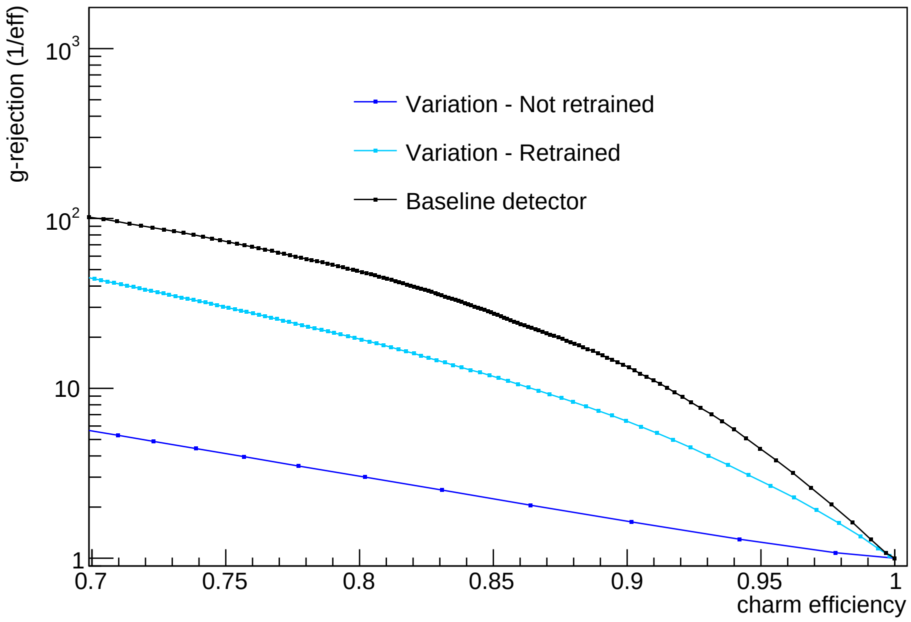

Figure 1. Rejection of gluon-initiated jets as a function of the charm jet-tagging efficiency for the baseline IDEA detector (black), an alternative IDEA tracker without re-training (blue) and the same alternative tracker with re-training (light blue) of the ParticleNet algorithm. It is evident that training the algorithm on the corresponding detector-configuration features is necessary to access their potential.

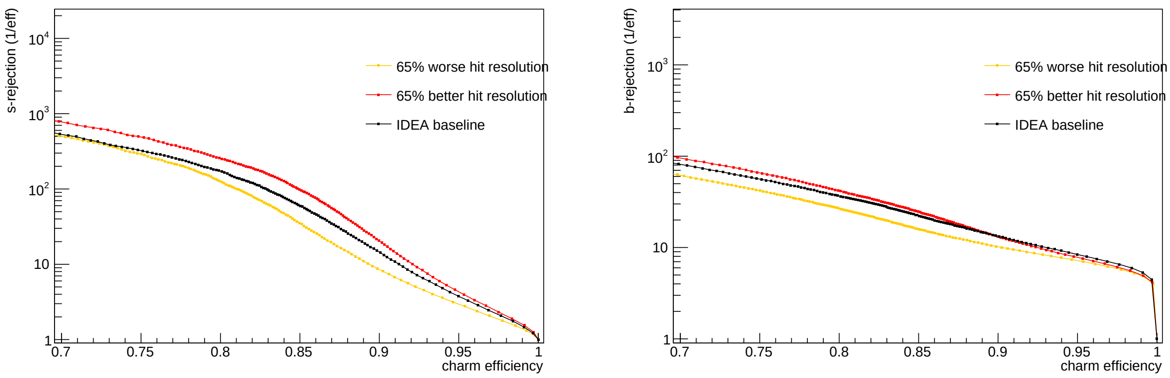

Figure 2. Rejection of strange(bottom)-initiated jets as a function of the charm jet tagging efficiency is shown on the left (right) for different hit resolutions.

2.2.2. *Silicon and beam-pipe material budget*

Tracking resolution may improve accuracy, as discussed in the previous sub-subsection, but often requires additional detector material. The impact of having more or less material in the vertex detector, as well as the interplay between beam-pipe and vertex-detector material budgets is discussed in this sub-subsection.

The standard radiation length for Silicon is assumed to be 0.0937 m. We studied the impact of relative variations in the radiation length for all of the Silicon layers at the same time, equivalent to increasing or reducing the relative amount of material by 50%. An asymmetric impact is observed for c-tagging, see Fig. 3. The impact of such variations on b- and s-tagging proves to be minor.

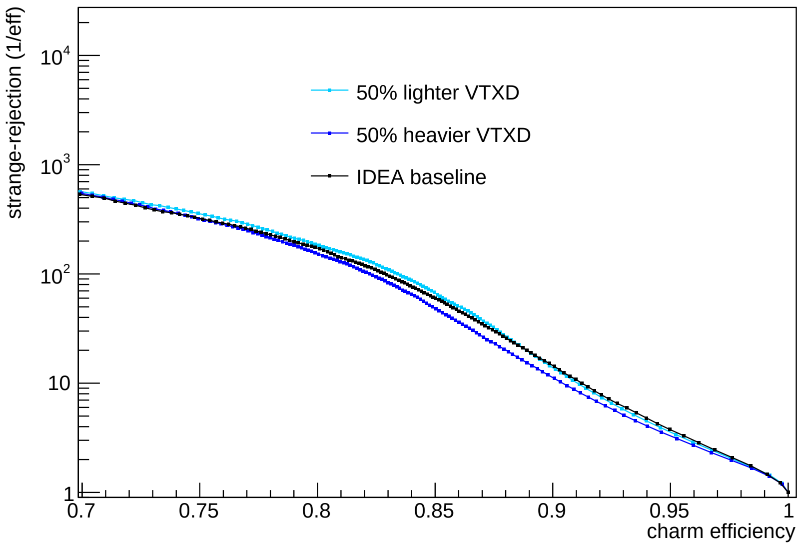

Figure 3. Rejection of strange-initiated jets as a function of the charm jet-tagging efficiency for different amount of material in the vertex detector: .

Overall these effects prove that there is not much to be gained from a lighter vertex detector, but performance can be easily affected by more or heavier material. These effects have been studied for jets whose momentum is above 70 GeV only and, as expected, the impact of multiple Coulomb interactions on performance becomes insignificant at high momentum. Furthermore, it has been observed that with a significant increase in beam-pipe material budget the impact of changes in the vertex-detector first layer material budget becomes sub-dominant.

2.2.3. *Removal of intermediate silicon layers*

The inclusion of an additional inner silicon layer plays a key role in c-tagging, as discussed in Ref. [6]. From these previous studies, an extra innermost layer brings minor improvements in b-tagging and improved background rejection in c-tagging. Since then, in the IDEA baseline detector concept the beam pipe was shrunk down to 1 cm and the four innermost silicon layer brought to: 1.2, 2, 3.15 and 15 cm from the beam axis, respectively. In this sub-subsection, we evaluate the impact on jet flavor tagging of removing the second or fourth innermost silicon layer.

As shown in Fig. 4, we expect visible effects on c-tagging. In particular, a larger impact is foreseen from the removal of the second, as compared to the fourth, innermost silicon layer. Similar patterns are observed in s, q and g rejection for c-tagging. Inclusively, b-tagging appears to be more robust against these changes, but it has to be noted that effects may become larger when considering jets produced at higher momentum (e.g. in differential measurements).

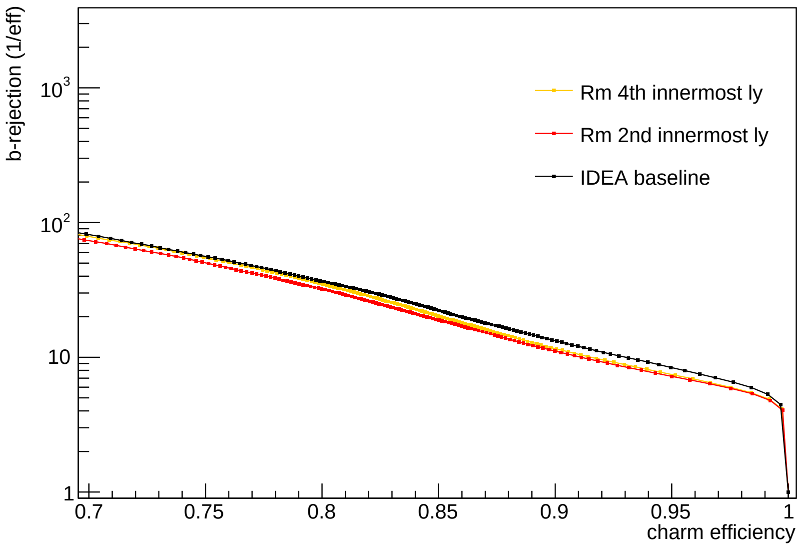

Figure 4. Rejection of bottom-initiated jets as a function of the charm jet tagging efficiency for the baseline IDEA vertex detector (black), the same without the second (red) and fourth (orange) innermost layer.

2.2.4. Drift chamber particle identification capabilities

A few variations in the amount and quality of PID information provided as input features to the algorithms training have been studied in order to characterize the flavor-tagging performance enhancement coming from each of these components and their combination: baseline PID, total absence of PID, absence of cluster-counting information, absence of TOF measurement, lack of both TOF and cluster-counting information, and baseline PID with improved timing resolution.

Figure 5 shows that the contribution of timing measurements to strange tagging is pretty limited in this kinematic regime. In fact, as discussed in Ref. [6] most of the TOF contributions to the PID separation between Kaons and pions is for a momentum within 1 and 2 GeV. On the other hand, effects due to the inclusion of TOF measurements are visible on charm tagging and significant on bottom tagging, both standalone and in combination with cluster-counting information.

Truth-matching of PF candidates to truth particles in Monte Carlo (MC) records has been implemented in order to study these effects and evaluate the superior limit on the performance enhancements due to the inclusion of PID information in the flavor-tagging algorithm. Figure 6 shows the multiplicity of truth-particle Kaons and the momentum of the leading Kaon, when at least one is produced, within Higgs-decay jets.

The truth-MC information, identifying charged-hadron and charged-lepton PF candidates within each jet, has been included in a dedicated training. The resulting improvement in performance is shown in Figure 7. As shown in Figure 6, bottom (charm) jets show a larger fraction of leading charged Kaons within the 1-to-2 GeV range than charm (strange) jets, which reflects the hierarchy of the relative effects observed in the tagger performance.

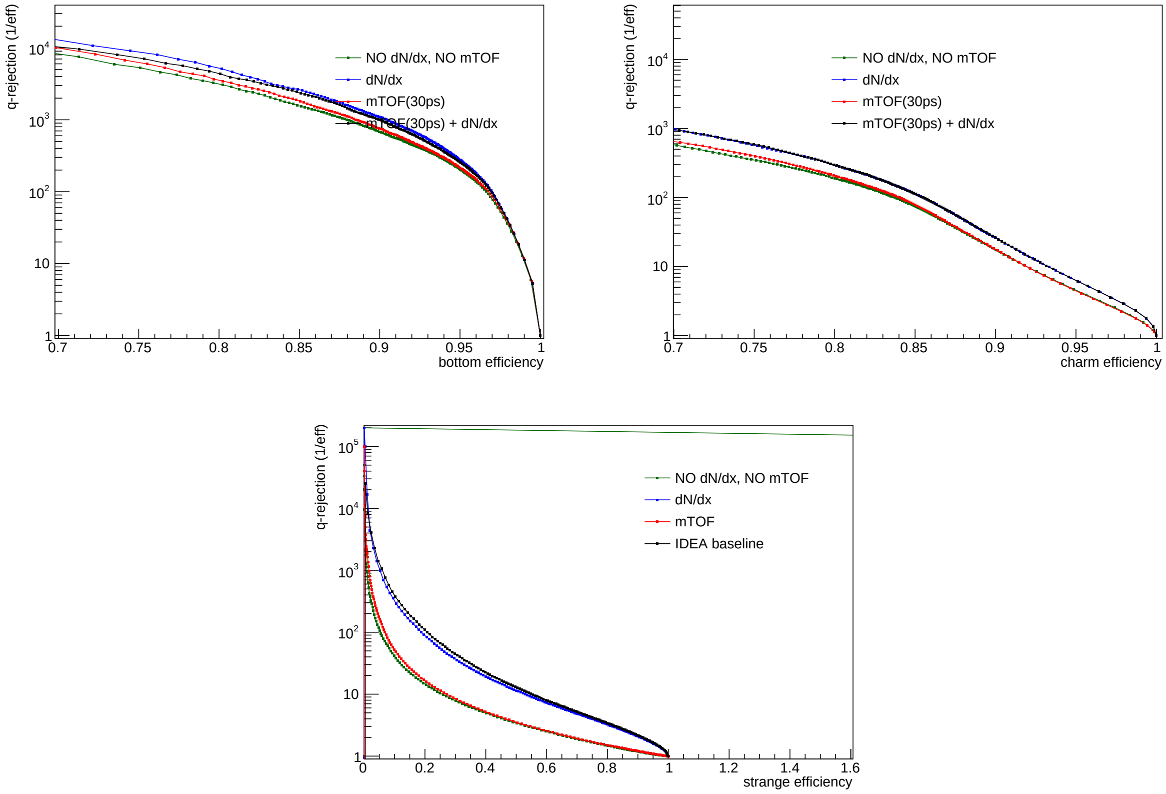

Figure 5. Rejection of light-initiated jets as a function of the strange jet tagging efficiency for the baseline IDEA vertex detector (black), the same without cluster counting (red), without TOF information (blue) and without both (green).

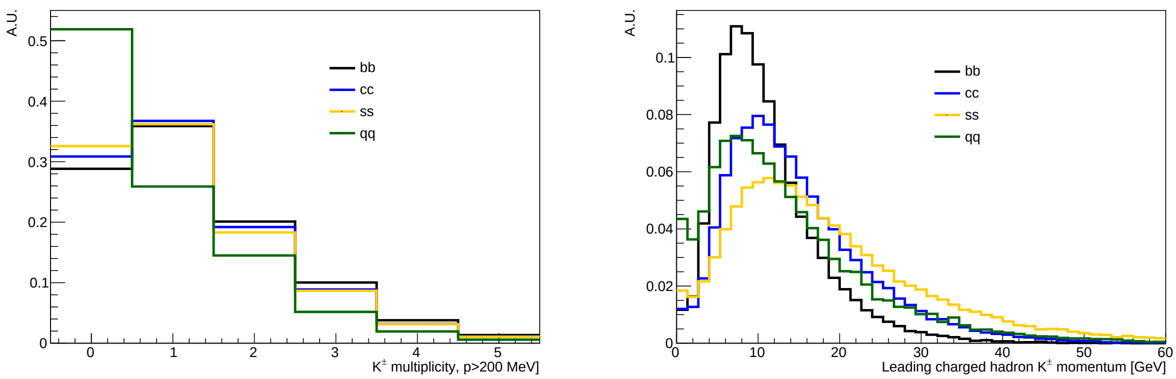

Figure 6. Multiplicity of Kaons with a minimum momentum of 200 MeV(left) in and momentum of the leading Kaon (right) within bottom (black), charm (blue), strange (yellow) and light (green) jets.

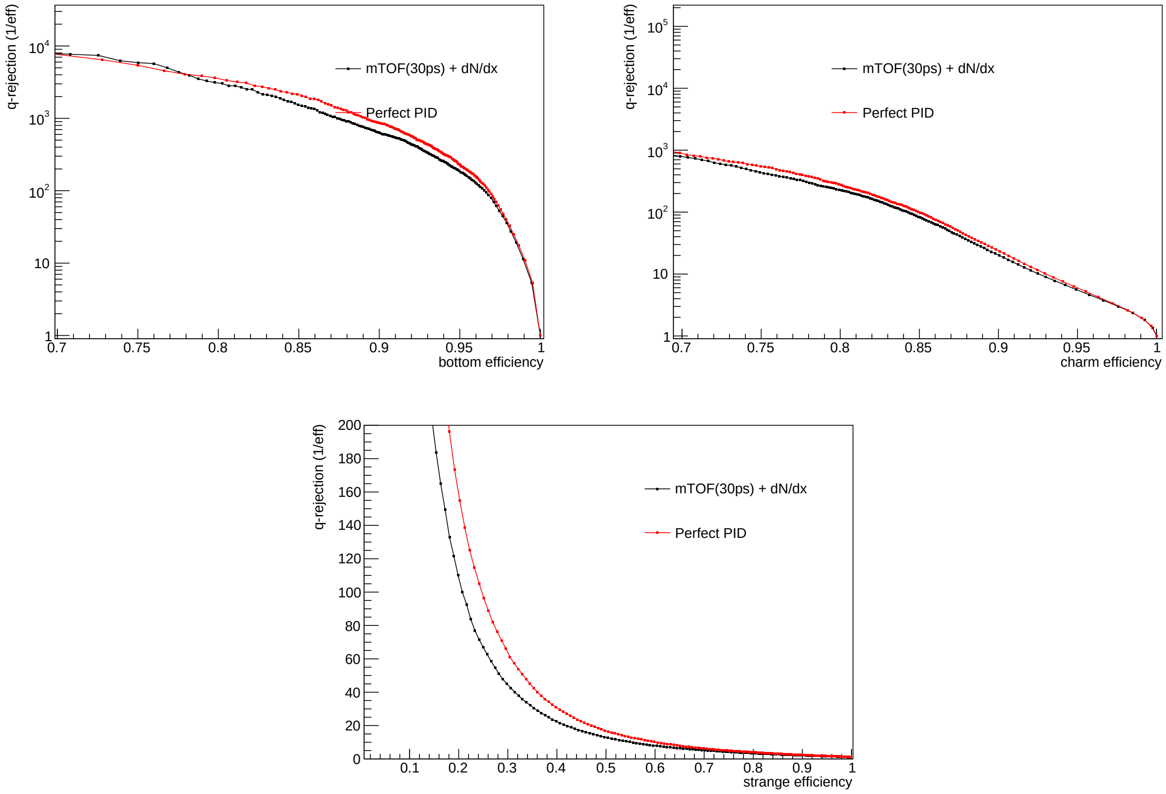

Figure 7. Light-rejection performance for bottom tagging (upper left), charm tagging (upper right) and strange tagging (bottom), and the baseline training (black) and a training including truth-MC information of charged-hadron and charged-lepton particle-flow candidates.

2.3. Variations in properties of calorimeter detectors

The nominal energy resolution for the IDEA prototype calorimeters has been assumed from Ref. [13]. In the electromagnetic crystal calorimeter:

$$\sqrt{a^2E^2 + b^2E + c^2} \tag{1}$$

with $a = 0.005$, $b = 0.03$ and $c = 0.002$.

In the hadronic dual-readout calorimeter:

$$\sqrt{d^2E^2 + e^2E + f^2} \tag{2}$$

with $d = 0.01$, $e = 0.3$ and $f = 0.05$. The nominal granularity of calorimeters is simulated by means of a cell size of about $6 \times 6\ cm^2$.

Energy-resolution parameters (a, b, c, d, e, f) are scaled up and down at the same time by a relative 30% to mimic potential degradation and improvement in the calorimeter performance. The nominal cell size is varied by a factor 2 in order to estimate the potential of a more or less granular calorimetry system.

3. ZH ANALYSIS IN THE FULLY HADRONIC FINAL STATE

The ZH fully hadronic analysis is rerun for each re-trained tagger, and the expected 68% Confidence Level uncertainty on the measured Higgs couplings to the b-, c-, s-quarks and the gluon are used as the metric to determine the impact of the flavour tagger's performance. The ZH fully hadronic analysis is described in the FCC note Ref. [14] and is briefly summarized in the following section.

3.1. Summary of the ZH analysis in the fully hadronic final state

The exclusive Durham kt-algorithm is used for jet clustering and requires each event to have exactly four jets, as both the Z and H decay hadronically. To reduce the backgrounds cuts on the angular separation between the jets are applied as follows, $15000 < d_{12} < 58000$, $400 < d_{23} < 18000$ and $100 < d_{34} < 6000$, where $d_{ij} = 2min(E_i^2, E_j^2)(1 - cos\theta_{ij})$ between the i^{th} and j^{th} jet. Additionally, the visible energy and mass are required to be greater than 150 GeV and the visible theta has to be within [0.15, 3.0]. Two or fewer leptons with the leading lepton having momentum less than 20 GeV are required on event level. Assuming that the jet directions are well measured and the initial energy of the final state is exactly known in a four-jet system the energy of the jets is corrected following energy and momentum conservation.

The flavour scores outputted by the flavour tagger are used to pair jets, which are identified as Z or H candidates based on their mass. Each jet has a flavour score roughly corresponds to the probability of the jet being initiated by a b-, c-, s-, u/d-quarks or gluon. Given jet i B_i, C_i, S_i, Q_i, G_i are the b-, c-, s-, q-, and g-flavour scores outputted by the flavour tagger. The maximum flavour score is found for each jet, and the pairing is done differently deepening on how many of the jet have the maximum flavour score from the same flavour. The five difference scenarios are handled as follows:

Case 1 - All jets with the same maximum flavour score In order to determine, which dijet pair forms the H/Z candidate all possible jet pairings are considered. For each paring $\chi^2_{comb} = \chi^2_Z + \chi^2_{Higgs}$ is computed, where $\chi^2_Z = (m_{Z,reco} - m_{\mathrm{Z\,true}})^2$ and $\chi^2_{Higgs} = (m_{H,reco} - m_{\mathrm{H\,true}})^2$. The jet paring that gives the minimum χ^2_{comb} is chosen as the correct one where $m_{Z/H,reco}$ are the reconstructed H/Z dijet masses. The H and Z bosons decay to the same flavour of jets.

Case 2 - Pairs with different maximum flavour score If after combining the jets with the same flavour maximum score the exactly two pairs are found of different flavour the Z candidate is simply chosen as the pair with minimum $\chi^2_Z = (m_{lk} - m_{\mathrm{Z\,true}})^2$, while the remaining pair is the H candidate.

Case 3 - Two jets with the same maximum flavour score Two jets with maximum score from the same flavour are paired, while the flavour of the second pair is determined by considering the same flavour score sums. The flavour of the second pair is taken as the flavour score that gives the maximum same flavour sum, $Max(\sum_{i,j} B, \sum_{i,j} C, ...)$. The H/Z candidates are determined as in Case 1 if both pairs have the same flavour or like in Case 2 if they are of different flavors.

Case 4 - Three jets with the same maximum flavour score Similarly as in Case 3 the first pair is found as the pair, which same flavour sum of scores is the greatest. The flavour of the second pair is then determined as in Case 3. The picking of the H/Z candidate follows the steps in Case 3.

Case 5 - Four different maximum flavour score If each jet has a maximum flavour score from a different flavour the event is not considered.

Finally additional cuts based on the mass of the H and Z candidates are applied in order to reject WW and ZZ background. The final fit is performed in the H and Z mass plane, where $50\,\mathrm{GeV} < m_{Z,reco} < m_{H,true}$ and $m_{H,reco} > m_{Z,true}$. There are in total 60 categories based on the flavor of the H and Z decay as well as the sum of the flavor score of the pair forming the Higgs candidates, i.e. purity categories.

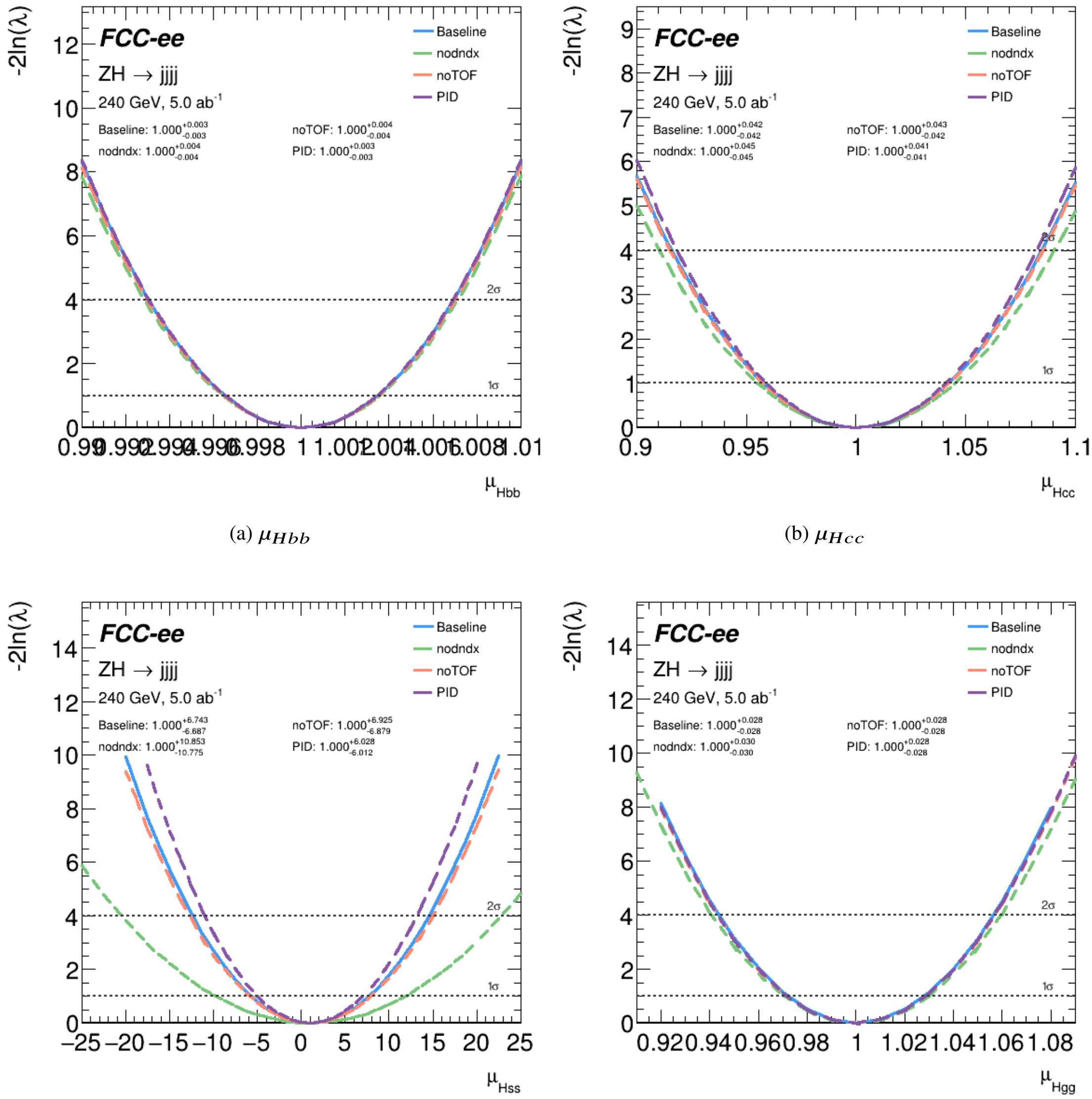

(a) μ_{Hbb}

(b) μ_{Hcc}

(c) μ_{Hss}

(d) μ_{Hgg}

Figure 8. Impact on the NLL scans from re-training the of the flavour tagger. The baseline training (blue line) and training without TOF information (orange line) have a similar performance when applied to the ZH fully hadronic analysis. However, the accuracy of identifying the dijet H/Z candidates degenerates when the tagger applied is not trained on the cluster counting information (nodNdx) leading to significantly worse limits μ_{Hss}. The precision of measuring μ_{Hcc} and μ_{Hss} improves assuming perfect PID (purple line) information is provided to the tagger, yet there is no expected improvement in measuring μ_{Hcc} and μ_{Hss}.

3.2. Impact of flavour tagger performance

While it has been shown in section 2.2 that the impact of the tagger performance is overestimated when evaluated on a simulation that differs from the one used in the training of the tagger this has a negligible impact on the analysis level. The assumption has been tested by applying the ParticleNet tagger trained on the baseline idea simulation and the ParticleNet tagger trained on the simulation with a 65% worse single hit resolution as compared to the baseline IDEA simulation applied to the ZccHbb, ZccHss, and ZccHgg signal samples generated both with the baseline and 65% worse single hit resolution detector geometry. It has been found that the tagging efficiency of the Higgs decay does not depend on the simulation the Particle Net tagger is applied to. This is likely due to the flavour tagging strategy used by the analysis in order to identify the flavour of the H and Z decay, which is proven to be robust. The effect observed in 2.2 is most prominent at lower tagging efficiencies, while taking the sum of the dijet flavour score ensures that the efficiency of flavour tagging is high and therefore the effect is not large.

Figure 8 shows the impact of the flavour tagger performance on the likelihood scan and subsequently the expected 68% Confidence Level uncertainty on the Higgs coupling to the b-, c-, s-quarks and gluons. For clarity only the impact of the tagger trained on the baseline IDEA detector, the case when the time of flight information (noTOF) or the cluster counting (nodNdx) is removed as an input to the training of the neural net. The scenario where the flavour algorithm training includes truth-level PID information (perfect PID) is also shown. It has been found that removing the innermost silicon layer, having displaced silicon barrel layers, 50% heavier or lighter vertex detector, or 65% better/worse single hit resolution does not impact the precision measurements of the Higgs couplings significantly, as expected from the ROC curves in Figures 2, 3, and 4. Similarly, the Higgs decay flavour reconstructed does not change notably when tagging with no time of flight information (noTOF) as can be seen in Figure 8. The reason for this is that the analysis is very robust due to the flavour tagging technique used, which determines the H/Z flavour with a high efficiency where different detector geometries have a lesser impact on the ParticleNet re-training, as can be seen from the ROC curves in Figure 5. Figure 9 shows that indeed the Higgs decay flavour reconstructed does not change notably when tagging with no TOF information. On the other hand, the lack of cluster-counting information (no dNdx) in the training of the tagger does impact the measurements of Higgs couplings. In the absence of the cluster-counting the expected uncertainty on $\mu_{H\to s\bar{s}}$ at 68% Confidence Level is 1.6 times worse as compared to the baseline uncertainty. The results are as expected from a closer inspection of Figure 5, which shows that the light jet rejection as a function of s-tagging efficiency takes a notable hit with no dNdx information as compared to the baseline tagger or missing TOF information. The smaller impact on the measured μ_{Hbb} and μ_{Hcc} as compared to μ_{Hss} in the no dNdx case is because the light jet rejection is significantly lower at high s-efficiency in contrast to the behavior observed at high b- and c-efficiencies. As outlined in Ref. [6] and Section 2.2.4 the results can be explained by considering the leading kaon momentum distribution in Figure 6. As expected from Figure 7 including truth PID information in the tagger training does not bring much improvement in the measurement accuracy. The largest gain is in determining $\mu_{H\to s\bar{s}}$, where the expected uncertainty on $\mu_{H\to s\bar{s}}$ improves 0.9 times as compared to the baseline IDEA concept. Table 2 summarizes the relative change in the expected uncertainty at 68% Confidence Level of the Higgs couplings due to retraining the Particle Net tagger on various detector-geometries compared to the baseline Particle Net tagger training.

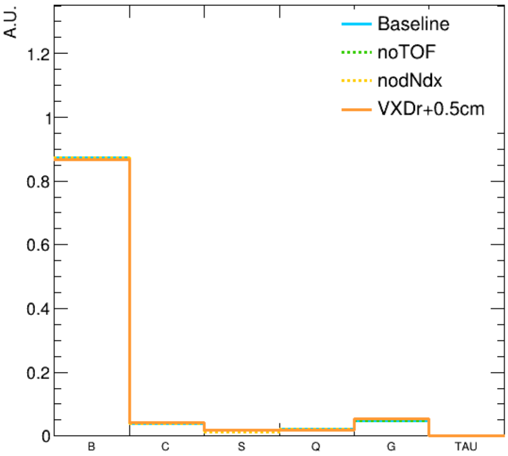

(a) True $H \to b\bar{b}$ events

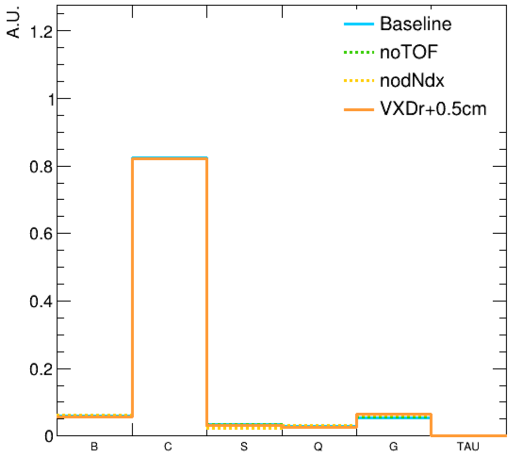

(b) True $H \to c\bar{c}$ events

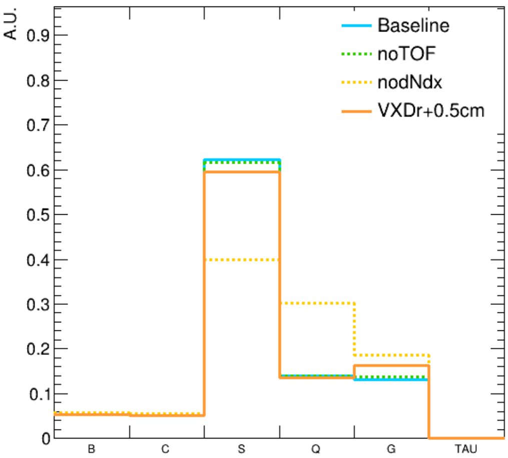

(c) True $H \to s\bar{s}$ events

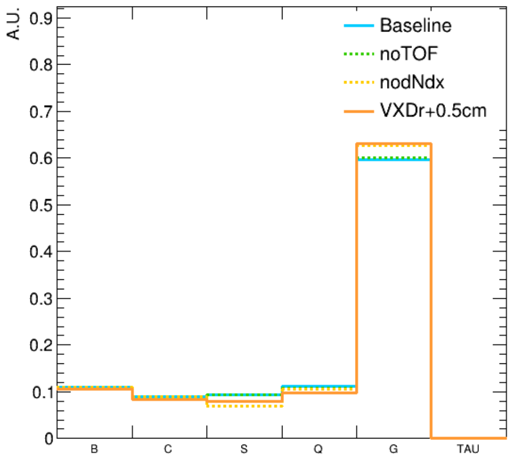

(d) True $H \to gg$ events

Figure 9. The categorization of the events based on the flavour of the reconstructed Higgs decay is shown. Reconstructed $H \to b\bar{b}$ decays are labeled as B, $H \to c\bar{c}$ as C, $H \to s\bar{s}$ as S, $H \to q\bar{q}$ as q, $H \to g\bar{g}$ as G and $H \to \tau\bar{\tau}$ as TAU. The tagger trained on the baseline IDEA detector (blue), no TOF information (green) and no dNdx information (yellow) and changing the beam pipe parameters are applied to the ZH fully hydroponic analysis and their performance evaluated. Only removing the dNdx information from training has a notable effect in reconsidering the H decayed. To be exact mis-identification of $H \to s\bar{s}$ decays as $H \to g\bar{g}$ or $H \to q\bar{q}$ events increases for about 20% as seen in (c).

	68% CL precision			
	μ_{Hbb}	μ_{Hcc}	μ_{Hgg}	μ_{Hss}
Baseline	±0.3%	±4.2%	±2.8%	+674% -669%
Relative change compared to baseline ($\mu_{variation}/\mu_{baseline}$)				
No TOF	x1.3	x1.02 (upper limit only)	x1	x1.03
No dNdX	x1.3	x1.07	x1.07	x1.6
Perfect PID	x1	x0.98	x1	x0.9

Table 2. Summary of the relative changes in the expected uncertainty at 68% Confidence Level of the Higgs coupling strengths extracted from the ZH fully-hadronic analysis. The first row shows the expected uncertainty at 68% Confidence Level on $\mu_{H\to b\bar{b}}$, $\mu_{H\to c\bar{c}}$, $\mu_{H\to gg}$ and $\mu_{H\to s\bar{s}}$ to which the results using the re-trained Particle Net tagger is applied are compared. The Particle Net tagger trainings where no time-of-flight (TOF) and no clustering information (no dNdx) are fed to the tagger are considered separately. The perfect PID represents the training where the truth PID information is considered in the training.

3.3. Comparing clustering algorithms in fully hadronic ZH events

The exclusive Durham-kt jet clustering algorithm set to n-jets mode has been used to reconstruct jets throughout the FCC feasibility studies. Motivated by the miss matching of jet pairs and miss clustering of soft particles that occurs in $e^+e^- \to ZH$ Higgs production using the Durham-kt algorithm, this study implemented the anti-kt clustering algorithm to compare the reconstructed Higgs mass resolutions in the fully hadronic 4-jet final state. The inclusive anti-kt algorithm was selected as a prospective alternative to the Durham-kt algorithm since it is infrared and collinear safe leading to reliability with soft or closely spaced particles. ZH events where the H decays to a pair of b quarks and the Z decays to a pair of c quarks were used to compare the efficacy of the clustering algorithms in a fully hadronic 4-jet final state. The anti-kt energy recovery algorithm outlined in the reference [15] slides was applied to events with more than four jets by first selecting the four hardest jets and then merging each soft jet with the hard jet that is closest in angle. A 10 GeV minimum energy threshold was then applied after the jets were merged. The anti-kt clustering algorithm was applied to the data with jet radius R varying from 0.4 to 1.0. As evident from Figure 10, the reconstructed Higgs mass using the anti-kt algorithm had the best mass resolution with radius 1.0 and the mean Higgs invariant mass was 125.0 GeV. The same figure displays that the mean Higgs invariant mass for the Durham-kt algorithm was 123.08 GeV. Ongoing studies are investigating why the R=1.0 radius produced the best results for the anti-kt algorithm.

4. HIGGS SELF-COUPLING INTERPRETATION

The Higgs self-coupling is a parameter of major interest, as it has a direct impact on the shape of the Higgs potential. It also has an SM predicted value, determined by the Higgs mass and vacuum expectation value, to which measurements at colliders can be compared to. This parameter is directly accessible through Higgs Pair Production (HH), a process actively studied at the LHC. It is possible to produce HH at an e^+e^- collider and access the Higgs self-coupling via the Higgs-strahlung process, provided that the e^+e^- center-of-mass energy is large enough. At the 240 GeV phase of FCC-ee, $\sqrt{s}$ is too low to produce HH. Instead, the Higgs self-coupling can be indirectly accessed through higher order contributions to the single Higgs process, allowing for the Higgs self-coupling to be probed using the ZH process, which will be abundant during

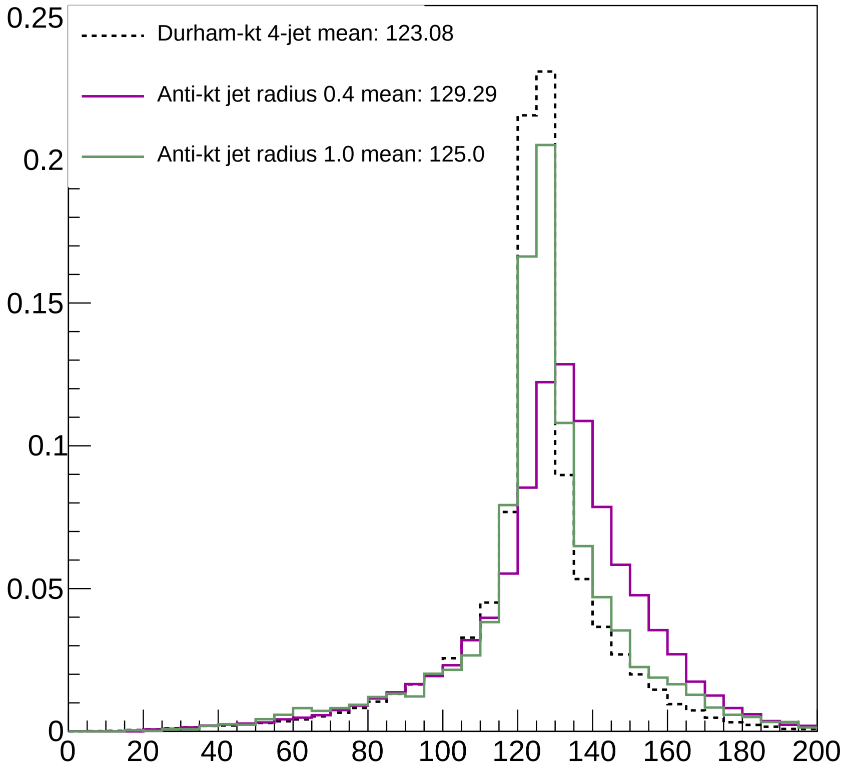

Figure 10. Comparing reconstructed Higgs mass with Durham-kt clustering set to 4-jets mode and anti-kt clustering set to jet radius $R = 0.4$ and $R = 1.0$.

the 240 GeV phase of FCC-ee. In general for e^+e^- colliders, the cross-section for HH starts to become experimentally viable around $\sqrt{s} = 500$ GeV.

The ZH cross-section can be parameterized as a function of the Higgs self-coupling through the kappa framework [16]. The parameterization can then be re-written in terms of a parameter from the SMEFT (SM Effective Field Theory) in the Warsaw basis [17], C_ϕ [18] [19], which affects the Higgs self-coupling via a dimension-6 operator. The following equation is used to parameterize the ZH cross-section as a function of C_ϕ:

$$\frac{\sigma_{\text{SMEFT}}(C_\phi, \sqrt{s} = 240\,\text{GeV}, \Lambda = 1\,\text{TeV})}{\sigma_{\text{SM}}} = \frac{1 + 0.017(0.47C_\phi)}{1 + 0.00154(0.47C_\phi)^2} \tag{3}$$

Only the cross-section of the ZH process is parameterized, while the branching ratios of different ZH processes are left at their SM values.

As described in Sec. 3, the fully hadronic ZH process can be used to study various Higgs couplings, and has been performed in [14]. For the interpretation described in this section, the same events passing the selections and categorization of the nominal full hadronic ZH analysis described in [14] are used, with the ZH cross-section parameterized as a function of C_ϕ using Eq. 3. This parameterization changes the cross-section in a linear fashion, up to about 0.8%, when varying C_ϕ from -1 to 1.This range of C_ϕ is considered accurate without including higher order terms in its expansion, as including higher powers of C_ϕ returns almost the same cross-section variation in this range. Additionally, setting C_ϕ to 0 leaves the cross-section unaltered, at its SM value.

This is applied to all ZH processes, and a likelihood scan is performed for the three detector variations described in Section 3.2. The result is shown in Fig. 11.

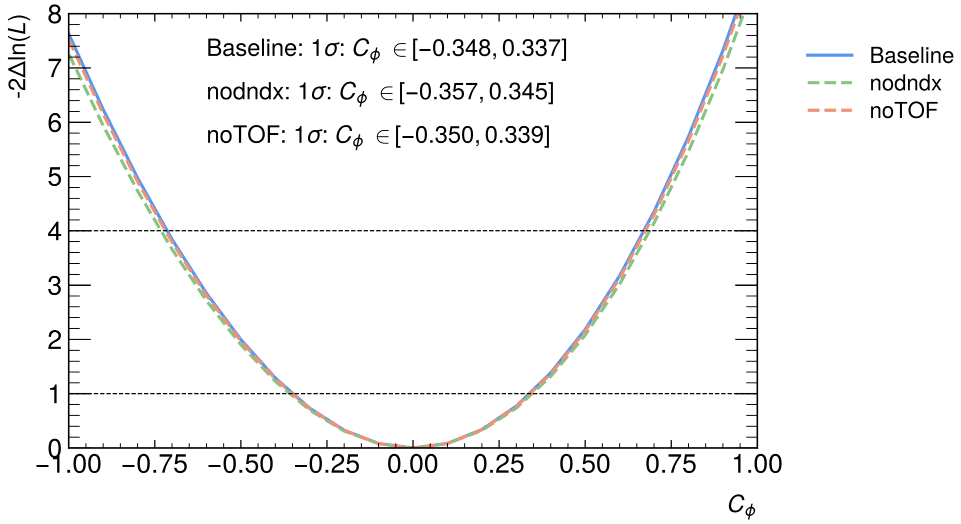

Figure 11. Likelihood scan as a function of C_ϕ .

Very similar behavior is seen for the other Higgs coupling scans shown in Fig. 8. This is expected as the same events are used for this interpretation as the coupling scans shown in Fig. 8, and the variation of the cross-section from C_ϕ is only up to about 0.8%.

It makes sense that similar constraints are seen for C_ϕ among different detector variations, as it is expected that the detector variations described in Section 3.2 have the largest impact on the coupling of the Higgs to strange quarks. All categories are included in the Higgs self-coupling interpretation in order to maximize sensitivity, among which the Higgs to strange quarks category is sub-dominant, and therefore does not strongly impact the combined C_ϕ constraint among different detector variations.

5. HIGGS-TO-INVISIBLE ANALYSIS

An important process to study at the FCC-ee is the invisible decay of the Higgs boson; many models of new physics predict contributions to this beyond the SM process $H \to ZZ \to 4\nu$. The very clean environment provided by electron-positron collisions allows reconstructing an unobserved Higgs boson decay using energy-momentum conservation and the known initial state. Therefore, this measurement is very sensitive to the detector design and simulation.

This is explored here in two ways. First, in Sections 5.1 to 5.6, the earlier analysis [20] that relied on fast simulation (for the IDEA detector [2, 3]) is updated to use full simulation (for the CLD detector [4]) for the signal and most of the backgrounds. This allows to explore differences between the fast and full simulation. Second, in Section 5.7, fast simulation of the IDEA detector is used to quantify the effect that the variations of the calorimeter properties described in Section 2.3 have on this measurement.

5.1. Samples with full simulation

All samples were generated with Whizard 3.1.2 [7, 21], with Pythia 6 [22] used for hadronization. The beam energy was set to $\sqrt{s} = 240$ GeV, and other beam setup parameters were copied from the configurations used for the winter 2023 production (branch `winter2023` in [23]), except that the vertex smearing was applied at the simulation step rather than at generation (to avoid crashes during simulation).

For the $Z(H \to 4\nu)$ signal samples, as well as other ZH backgrounds, the desired decay mode of the Higgs boson was selected using the `unstable` feature of Whizard. For the ZZ samples, the desired process was selected using the "restriction" feature of Whizard. In addition, the generated Z resonance was required to be within 5 GeV of the SM value.

For the ZH and $Z \to \tau\tau$ samples, the cross sections and branching ratios were taken directly from Whizard and the Particle Data Group [24]. For the ZZ samples, however, the cross sections calculated by Whizard were about 40% less than those calculated by Pythia8 [25] for the winter 2023 production. As the cause of this discrepancy was not identified, the cross sections calculated by Whizard were scaled by a factor of 1.44 to match the earlier production. Backgrounds not covered by the full simulation were taken from the winter 2023 fast simulation, including the entire WW sample. Where needed, Monte Carlo generator information was used to exclude subprocesses covered by full simulation in order to avoid double-counting. A summary of the samples generated is given in Table 3.

These samples were processed through the standard simulation of the CLD detector concept [4], which is implemented using Geant4 [26] and DD4hep [27]. Reconstruction used the `CLDReconstruction.py` and `PandoraSettingsCLD` [28] configurations from the `CLDConfig` [29] repository. All simulation and reconstruction used the 2023-11-23 release of Key4Hep [30].

Table 3. Samples generated for the full-simulation $H \to$ invisible analysis. $\ell \equiv e, \mu$. For each sample, the table shows the total number of events generated, the product of the cross section and branching ratio for the sample, and the number of events expected in 10.8 ab^{-1} of data both before and after the analysis selections described in Section 5.4.

Channel	Events generated	$\sigma \times$ BR (fb)	Events expected in 10.8 ab^{-1}	Events expected after selection
Signal				
$(Z \to e^+e^-)(H \to 4\nu)$	20 000	0.007 95	85.8	40.4
$(Z \to \mu^+\mu^-)(H \to 4\nu)$	20 000	0.007 39	79.8	57.0
$(Z \to q\bar{q})(H \to 4\nu)$	20 000	0.149	1600	1180
Background				
$(Z \to \nu\nu)(H \to e^+e^-\nu\nu)$	18 000	0.124	1330	34.5
$(Z \to \nu\nu)(H \to \mu^+\mu^-\nu\nu)$	18 000	0.124	1340	47.9
$(Z \to \nu\nu)(H \to q\bar{q}\nu\nu)$	18 000	0.316	3420	1040
$(Z \to \nu\nu)(H \to q\bar{q})$	18 000	27.7	300 000	21 100
$(Z \to e^+e^-)(Z \to \nu\nu)$	18 000	16.0	173 000	88 600
$(Z \to e^+e^-)(Z \to q\bar{q})$	18 000	54.6	589 000	26 400
$(Z \to \mu^+\mu^-)(Z \to \nu\nu)$	18 000	16.0	173 000	139 000
$(Z \to \mu^+\mu^-)(Z \to q\bar{q})$	18 000	54.6	589 000	35 600
$(Z \to q\bar{q})(Z \to \nu\nu)$	18 000	323	3 490 000	2 740 000
$(Z \to q\bar{q})(Z \to q\bar{q})$	18 000	516	5 570 000	$<$ 310
$(Z \to \tau\tau)$	5 150 000	4668	50 400 000	899 000

5.2. Effect of the FCC crossing angle

At the FCC, each beam enters the detector with an angle of 0.015 rad with respect to the z-axis in the horizontal plane, giving a total crossing angle of 0.030 rad. This gives a boost to the entire event in the x-direction of $\beta = \sin(\theta/2)$. Figure 12 shows the total momentum in the x-direction for $ZZ \to qqqq$ events. It is seen that the distribution is offset from zero by several GeV. As this would affect the reconstruction of missing momentum, all final state particles in fully-simulated samples are boosted in the x-direction to compensate for this.

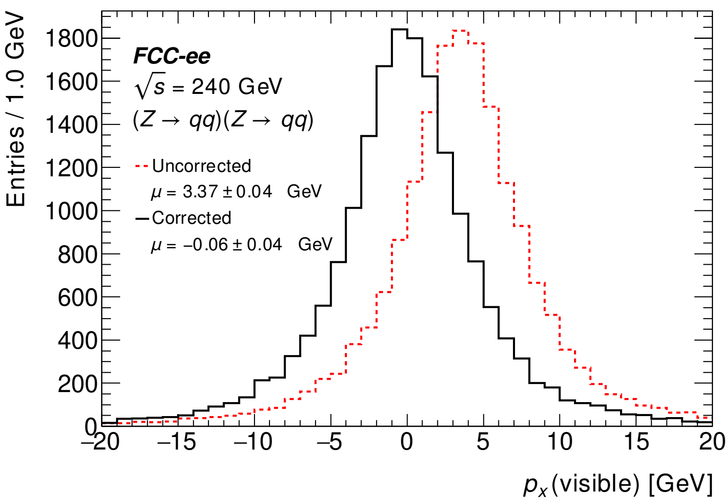

Figure 12. Total sum of the momenta of final-state particles in the x-direction, for $ZZ \to qqqq$ events. The dashed curve shows the sum before applying the boost, and the solid curve shows the sum after the correction.

This effect is not implemented in the fast simulation; this correction was not applied for those samples.

5.3. Bremsstrahlung recovery

Electrons traversing the detector radiate photons at small angles (bremsstrahlung), leading to a large low-mass tail in the m_{ee} distribution, shown by the dashed curve in Fig. 13a. As this effect is not included in the fast simulation, and is not accounted for in the standard CLD reconstruction, this represents a significant contribution to differences seen between fast and full simulation. To reduce these differences, a correction for bremsstrahlung was made during the analysis.

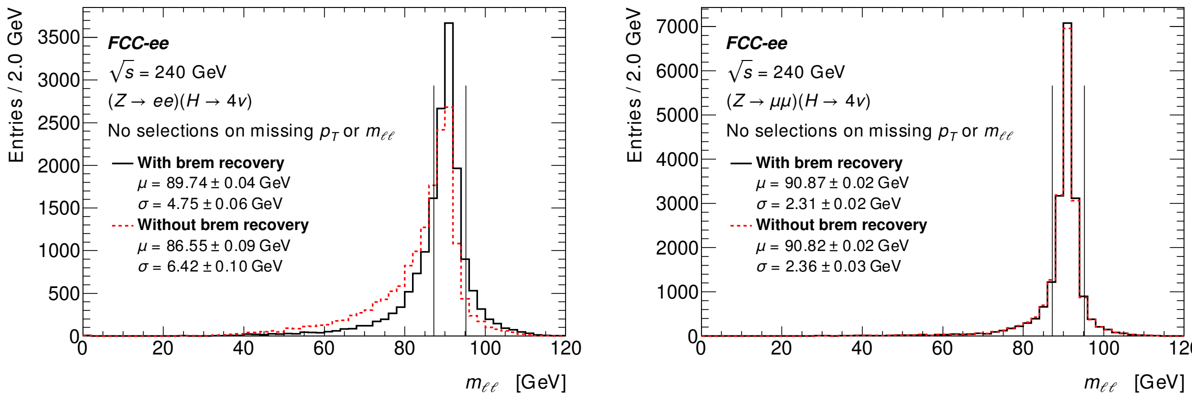

(a) (b)

Figure 13. Dilepton pair invariant mass for ZH events with the Higgs boson decaying to four neutrinos and the Z boson decaying to (a) electrons and (b) muons. The dashed curve shows the distribution without correcting for bremsstrahlung, and the solid curve shows the distribution with the correction. The means and widths of Gaussian functions fit to the distributions are also shown. Vertical lines delimit the range accepted by the analysis selection.

Doing the correction at analysis level implies that refitting tracks is not feasible. Instead, the analysis finds the highest-momentum photon candidate within a 0.05 rad cone around each lepton. It then remains to decide whether or not to add the momentum of that photon to that of the lepton.

Always adding the photon to the lepton makes the resolution worse: depending on where in the detector the photon was radiated, its momentum may already have been included in the lepton's track. Instead, a neural network (NN) is trained to discrimate the cases in which the photon should be added. Leptons are classified based on whether adding the photon brings the lepton's momentum closer to or further from the momentum given by MC truth information. If adding the photon brings the momentum closer to the MC truth, the photon is classified as 'signal,' meaning it should be added to the lepton. Otherwise, the photon is classified as 'background.'

The NN has five input variables, shown in Fig. 14:

- The lepton momentum p_ℓ;
- the lepton polar angle θ_ℓ;
- the angle between the lepton and photon $\Delta\theta(\ell, \gamma)$;
- the energy of the lepton's calorimeter cluster E_ℓ^{calo}; and
- the energy of the photon's calorimeter cluster E_γ^{calo}.

A NN is trained using the DNN method from TMVA [31] with two hidden layers containing 14 and 6 nodes, respectively. The hidden layers used tanh activation functions, while the output node used a linear activation function. The $(Z \to ee)(H \to 4\nu)$ signal sample was used for training, evenly split into training and test samples. The NN output is shown in Fig. 15.

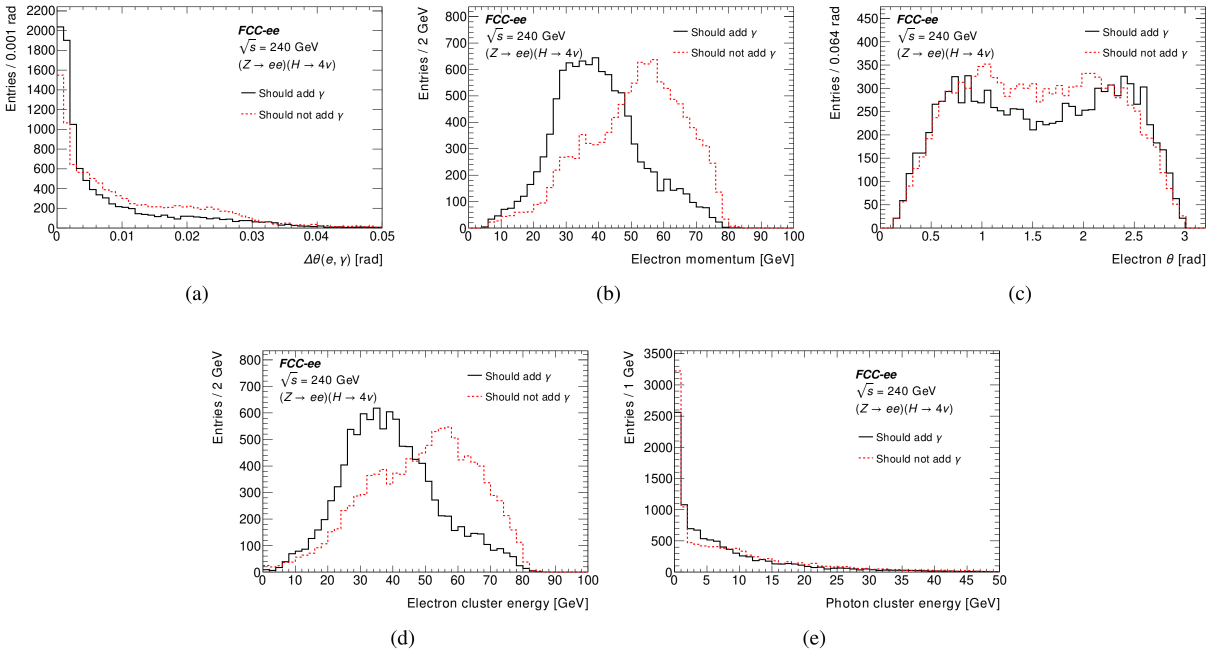

Figure 14. Variables used as input to the NN to determine whether or not to add a photon to a lepton for bremsstrahlung recovery. Shown for electrons in the $(Z \to ee)(H \to 4\nu)$ sample. (a) Angle between the electron and photon; (b) Electron three-momentum; (c) Electron polar angle (θ); (d) Energy of the electron's calorimeter cluster; (e) Energy of the photon's calorimeter cluster. In each case, distributions are shown for the population for which adding the photon inproves the measurement (solid line) and those for which adding the photon worsens the measurement (dashed line).

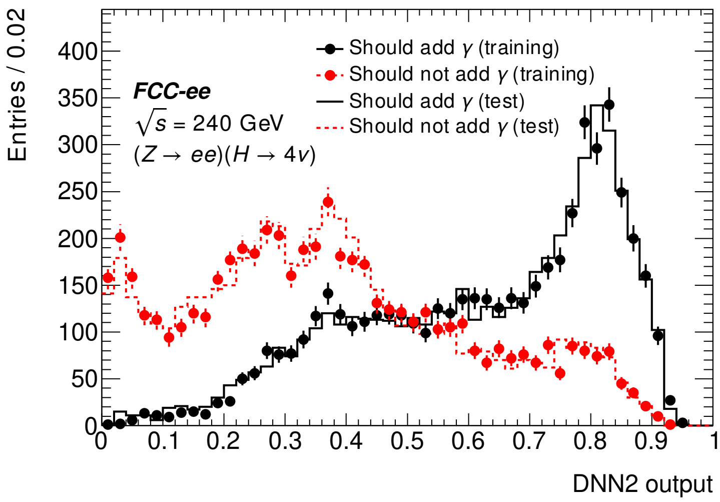

Figure 15. Output of the NN for bremsstrahung recovery, shown for electrons in the $(Z \to ee)(H \to 4\nu)$ sample. The test samples are shown as curves; the solid curve is the for the population for which adding the photon inproves the measurement and the dashed curve is those those for which adding the photon worsens the measurement. The corresponding training samples are shown as points.

Table 4. Summary of event selection for the invisibly-decaying Higgs boson analysis with full simulation.

Leptons	Tight electrons or muons with $p > 10\,\text{GeV}$ Apply bremsstrahlung recovery	
Channel definition	Exactly two leptons: e^+e^- or $\mu^+\mu^-$	No leptons
Missing p_T	$p_{T,\text{vis}} > 10\,\text{GeV}$	$p_{T,\text{vis}} > 15\,\text{GeV}$
Z boson decay	$\lvert m_{\ell\ell} - M_Z \rvert < 4\,\text{GeV}$	$86\,\text{GeV} < m_\text{vis} < 105\,\text{GeV}$

If the NN output is greater than 0.5, then the photon is added to the lepton. The result for electrons is shown in the solid curve of Fig. 13a. The distribution narrows and becomes more symmetric, as the mean moves closer to the mass of the Z boson. The same NN is also applied to muons, although they are much less affected by bremsstrahlung than are electrons. This is shown in Fig. 13b; even for muons, the width of the distribution narrows slightly.

5.4. Selection and analysis

The selection used here is based on that of the previous analysis based on fast simulation only [20], updated for use with full simulation.

First, all final-state particles are boosted into the center-of-mass frame, as outlined in Section 5.2. Next, electrons, muons, and photons are selected using the tight selections provided by PandoraPFA. Elecrons and muons must have three-momenta $p > 10\,\text{GeV}$, and in addition must be isolated. For each lepton, calculate the scalar sum p_cone of the three-momenta of all final-state particles within a cone of $0.01 < \Delta R < 0.5$, where $\Delta R = \sqrt{(\Delta\phi)^2 + (\Delta\eta)^2}$ and η is the pseudorapidity. A lepton is considered isolated if $p_\ell / p_\text{cone} > 0.5$. Next, bremsstrahlung recovery is applied to the leptons, as outined in Section 5.3. Finally, the momenta of all final state particles are summed to obtain the total visible momentum, p_vis. Photons that the bremsstrahlung recovery NN determined should not be added to their associated leptons are excluded from this sum. The procedure is similar for the backgrounds for which fast simulation is used, except that the overall boost to the center-of-mass frame and bremsstrahlung recovery are not performed, and electrons and muons are selected using the provided lists.

The analysis is divided into three channels, electrons, muons, and hadrons, depending on the decay of the Z boson. For the leptonic channels, there must be exactly two same-flavor, opposite-sign leptons, $p_{T,\text{vis}} > 10\,\text{GeV}$, and $\lvert m_{\ell\ell} - M_Z \rvert < 4\,\text{GeV}$. For the hadronic channel, there must be no identified leptons, $p_{T,\text{vis}} > 15\,\text{GeV}$, and $86\,\text{GeV} < m_\text{vis} < 105\,\text{GeV}$. This selection is summarized in Table 4. For the hadronic channel, the range of the visible mass selection is significantly larger than was used in the previous analysis based on fast simulation [20]. The visible mass distribution for the hadronic channel is shown in Fig. 16. In contrast to the $m_{\ell\ell}$ distributions shown in Fig. 13, this distribution peaks significantly above the mass of the Z boson. This may be due to confusion in PandoraPFA, where neutral cluster near a charged hadron is reconstructed as a separate photon despite its momentum being included in the charged hadron's track, resulting in double-counting its energy in the sum over all particles.

Finally, the recoil mass is calculated from the total visible momentum and the nominal collision energy. The result is shown for the three channels in Fig. 17.

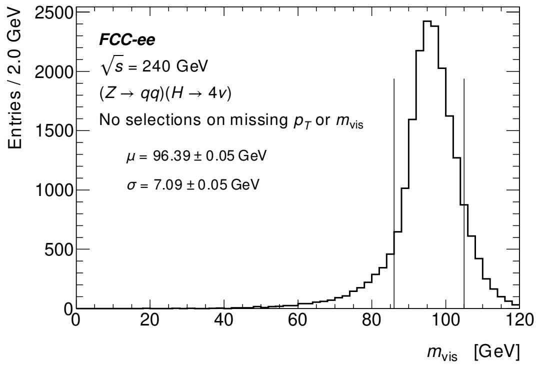

Figure 16. Invariant mass of all visible particles for ZH events with the Higgs boson decaying to four neutrinos and the Z boson decaying hadronically. The mean and width of a Gaussian function fit to the distribution is also shown. Vertical lines delimit the range accepted by the analysis selection.

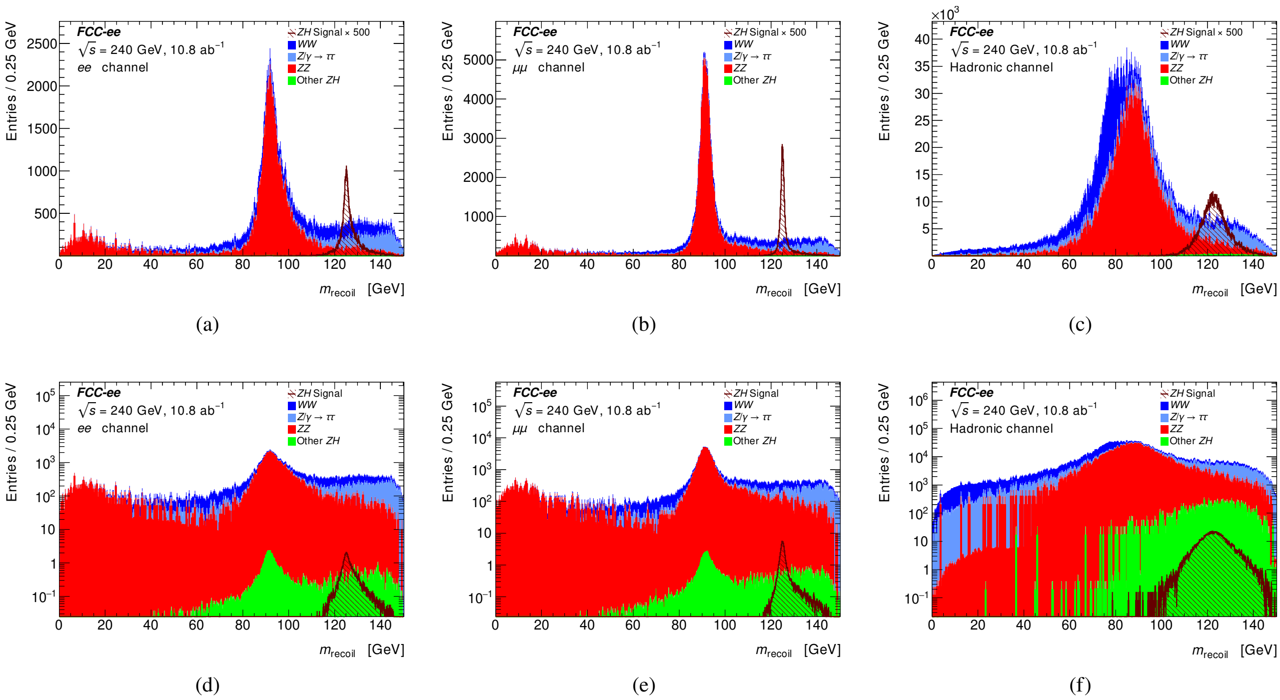

Figure 17. Distribution of reconstructed invisible recoil mass after all selections normalized to an integrated luminosity of 10.8 ab^{-1} for the signal and backgrounds available with full simulation for the (a, d) ee, (b, e) $\mu\mu$, and (c, f) hadronic channels. (a–c) are shown with a linear scale with the signal cross section multiplied by a factor of 500, while (d–f) are shown with a logarithmic scale.

5.5. Resolution study between fast simulation and full simulation

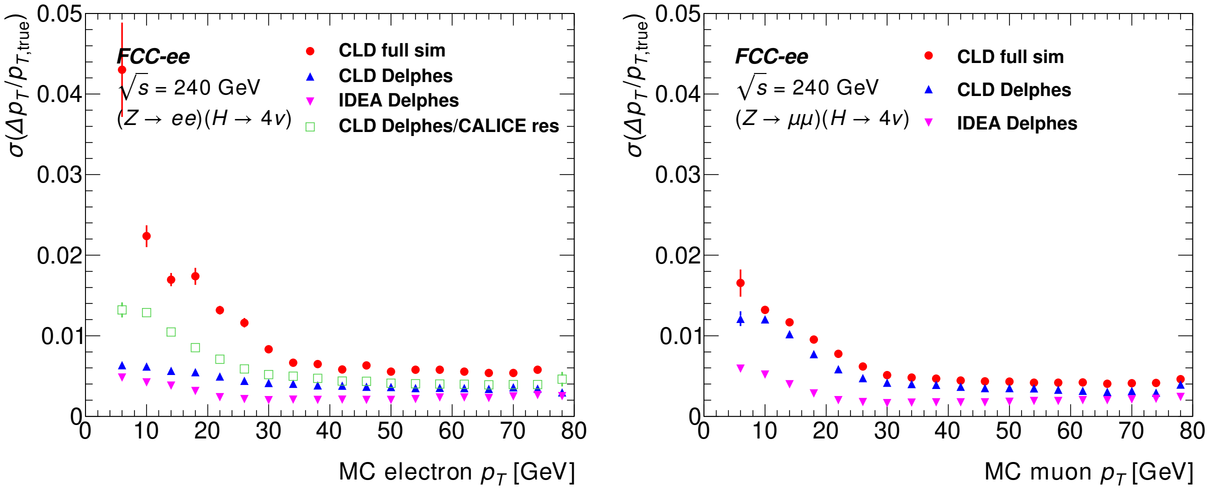

(a) (b)

Figure 18. Relative transverse momentum resolution as a function of transverse momentum for (a) electrons and (b) muons. Within each transverse momentum bin, the resolution distribution is fit to a Gaussian distribution. Shown are results from full simulation (Bremsstrahlung recovery is not applied), fast simulation for both CLD and IDEA configurations, and fast simulation for CLD with the calorimeter resolution function replaced with the expected resolution for a silicon-tungsten CALICE-like calorimeter.

Figure 18 shows the transverse momentum resolution seen for electrons and muons in full simulation compared with fast simulation using both the CLD and IDEA configurations. For muons, the momentum resolution is determined almost entirely by the tracking resolution. The resolution from the CLD fast simulation is similar to that from the CLD full simulation. Further, the fast simulation for IDEA shows a significantly better momentum resolution than that for CLD. This is expected because the drift chamber-based tracking of IDEA has less material than the all-silicon tracker of CLD, with the biggest difference expected at low momenta where measurement errors are dominated by multiple scattering.

For electrons, however, the momentum resolution from the CLD fast simulation is much better than that from the CLD full simulation. In fact, the momentum resolution seen in the fast simulation is better for electrons than for muons, especially at low momenta. This is because the electromagnetic calorimeter resolution in the fast simulation configurations for both CLD and IDEA corresponds to that expected from a crystal calorimeter: $\sigma E/E = 0.5\% \oplus 3\%/\sqrt{E} \oplus 0.2\%/E$. However, CLD uses a silicon-tungsten CALICE-style calorimeter with an expected resolution of about $\sigma E/E = 1\% \oplus 16\%/\sqrt{E}$ [13]. Figure 18a shows also the result of replacing the calorimeter resolution in the CLD fast simulation with that expected from a CALICE-like calorimeter; the result is significantly closer to that from full simulation. Hence, one should use the existing fast simulation with care for uses that depend on the resolution of the electromagnetic calorimeter.

5.6. Statistical model and Limits

To determine the upper limit on the branching ratio ($\mathrm{BR}_{\mathrm{inv}}$) of the Higgs decaying into invisible final states, we employ the `xRooFit` toolkit. Only statistical uncertainties are considered. The likelihood function is constructed using signal and background models derived from simulation. The total probability density function (PDF) is expressed as a combination of the signal ($S(x)$) and background ($B(x)$) components:

Limit set on $\mathcal{B}(H \to \text{inv})$					
Channels	-2σ	-1σ	Limit	+1σ	+2σ
ee	5.2×10^{-3}	6.9×10^{-3}	9.7×10^{-3}	1.4×10^{-2}	1.8×10^{-2}
$\mu\mu$	2.2×10^{-3}	3.0×10^{-3}	4.0×10^{-3}	5.8×10^{-3}	7.8×10^{-3}
qq	2.5×10^{-3}	3.4×10^{-3}	4.8×10^{-3}	6.6×10^{-3}	9.0×10^{-3}

Table 5. Limit of on the Higgs to invisible branching ratio for different channels

$$P(x \mid \mu) = \mu \cdot S(x) + (1 - \mu) \cdot B(x), \tag{4}$$

where x represents the observable (the recoil mass in our case), and μ is the signal strength parameter. The signal strength is related to the branching ratio BR_{inv} by:

$$\mu = \frac{\sigma_{\text{obs}} \cdot \text{BR}_{\text{inv}}}{\sigma_{\text{SM}}}, \tag{5}$$

where σ_{obs} is the observed Higgs production cross-section, and σ_{SM} is the Standard Model prediction. To mimic experimental conditions, pseudo-datasets are generated by sampling the expected signal-plus-background or background-only distributions. These pseudo-datasets incorporate statistical fluctuations consistent with the expected event yields.

The profile likelihood ratio is used as the test statistic:

$$\lambda(\mu) = \frac{\mathcal{L}(\mu)}{\mathcal{L}(\hat{\mu})}, \tag{6}$$

where $\mathcal{L}(\mu)$ is the likelihood of the pseudo-data given the hypothesized signal strength μ, and $\hat{\mu}$ is the value of μ that maximizes the likelihood. The test statistic $-2\ln\lambda(\mu)$ is evaluated to compare the signal-plus-background hypothesis to the background-only hypothesis. The distribution of $-2\ln\lambda(\mu)$ under the background-only hypothesis is determined using asymptotic approximations. The upper limit on BR_{inv} at 95% confidence level (CL) corresponds to the value of μ where the cumulative probability of the test statistic exceeds the critical threshold for the chosen CL. The analysis yields an upper limit on BR_{inv} at 95% CL, based on statistical uncertainties alone. The exclusion curve, derived from the pseudo-data, provides the sensitivity of the analysis as a function of the signal-to-background ratio or integrated luminosity. Since systematic uncertainties are not considered, the results represent an idealized scenario with statistical errors only.

5.7. Detector variations

Variations in the calorimeter properties, as described in Section 2.3, have been propagated through the Higgs-to-invisible analysis [20]. Figure 19 presents the distribution of the reconstructed invisible recoil mass, normalized to the corresponding cross sections for the ZH signal. To assess the impact of different detector configurations on the Higgs-to-invisible sensitivity, we determined the limit on the Higgs-to-invisible branching ratio for each configuration.

Six detector configurations, corresponding to the signal distributions in Figure 19, were generated using fast simulation. For the background, the nominal detector configuration was used, also simulated with the fast simulation. Only the qq channel is considered in this study, as it provides the best sensitivity, as demonstrated in Table 5. The results of this evaluation are summarized in Table 6.

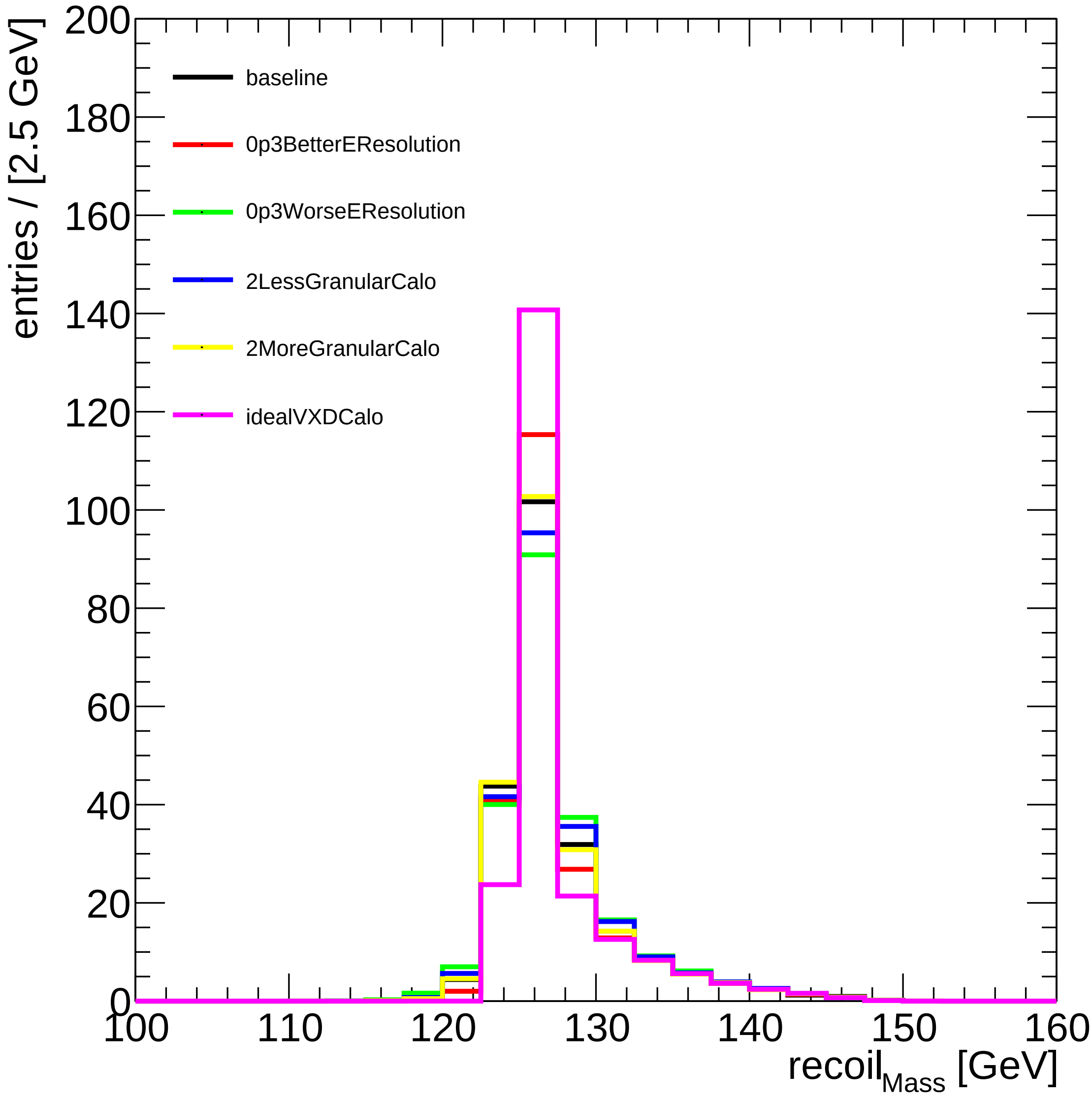

Figure 19. Distribution of reconstructed invisible recoil mass normalized to corresponding cross sections for ZH signal in the qq channel. Different calorimeter properties are compared: baseline IDEA calorimeter (black), a 30% better relative energy resolution (red), a 30% worse relative energy resolution (green), two times more granular (yellow) and two times less granular (blue) calorimeter.

Reletive limit on $\mathcal{B}(H \to \text{inv})$ in %					
Detector config	-2σ	-1σ	Limit	+1σ	+2σ
0p3BetterEResolution	-8.33	-12.12	-8.89	-9.52	-10.59
0p3WorseEResolution	+12.5	+9.09	+11.11	+11.11	+10.59
2LessGranularCalo	+8.33	+6.06	+6.67	+6.35	+5.88
2MoreGranularCalo	0.0	-3.03	0.0	0.0	-1.18
idealVXDCalo	-25.0	-27.27	-26.67	-26.98	-25.88

Table 6. Relative limit on the Higgs to invisible branching ratio compared to the baseline limit for different detector changes in %. Only qq channel is considered. The - (+) sign indicates the limit is better (worse) than the limit obtained using the baseline configuration of the detector.

6. CONCLUSION

The effect of different detector configurations on three main analyses at FCC-ee is presented. It was shown how different tracker configurations affect flavor-tagging performance and their implications on the measurement of the Higgs-boson couplings. For the Higgs couplings analysis new clustering methods have also been studied. Furthermore, variations of the calorimeter properties were propagated through the Higgs-boson-to-invisible search, where for the first time full simulation of the detector was used. This work can be used to understand the geometry and most optimal detector configuration for future experiments at FCC-ee.

ACKNOWLEDGEMENTS

This research was supported in part by the U.S. Department of Energy's Office of Science, Office of High Energy Physics under contract no. DE-SC0012704. This work was supported by resources provided by the Scientific Data and Computing Center (SDCC), component of the Computational Science Initiative (CSI) at Brookhaven National Laboratory (BNL).

References

[1] A. Abada et al. "FCC-ee: The Lepton Collider: Future Circular Collider Conceptual Design Report Volume 2". In: *Eur. Phys. J. ST* 228.2 (2019), pp. 261–623. DOI: 10.1140/epjst/e2019-900045-4.

[2] G. Gaudio. "The IDEA detector concept for FCCee". In: *PoS* ICHEP2022 (Nov. 2022), p. 337. DOI: 10.22323/1.414.0337.

[3] M. Antonello. "IDEA: A detector concept for future leptonic colliders". In: *Nuovo Cim. C* 43.2-3 (2020). Ed. by G. D'Ambrosio and G. De Nardo, p. 27. DOI: 10.1393/ncc/i2020-20027-2.

[4] N. Bacchetta et al. "CLD – A Detector Concept for the FCC-ee". In: (Nov. 2019). arXiv: 1911.12230 [physics.ins-det].

[5] J. Pekkanen. "ALLEGRO FCC-ee detector concept & Noble liquid calorimetry". In: *Nucl. Instrum. Meth. A* (2024), p. 169921. DOI: https://doi.org/10.1016/j.nima.2024.169921.

[6] F. Bedeschi, L. Gouskos, and M. Selvaggi. “Jet flavour tagging for future colliders with fast simulation”. In: *Eur. Phys. J. C* 82.7 (2022), p. 646. DOI: 10.1140/epjc/s10052-022-10609-1. arXiv: 2202.03285 [hep-ex].

[7] W. Kilian, T. Ohl, and J. Reuter. “WHIZARD: Simulating Multi-Particle Processes at LHC and ILC”. In: *Eur. Phys. J. C* 71 (2011), p. 1742. DOI: 10.1140/epjc/s10052-011-1742-y. arXiv: 0708.4233 [hep-ph].

[8] J. de Favereau et al. “DELPHES 3, A modular framework for fast simulation of a generic collider experiment”. In: *JHEP* 02 (2014), p. 057. DOI: 10.1007/JHEP02(2014)057.

[9] `TrackCovariance` module in DELPHES. URL: https://github.com/delphes/delphes/blob/master/modules/TrackCovariance.cc.

[10] `TimeOfFlight` module in DELPHES. URL: https://github.com/delphes/delphes/blob/master/modules/TimeOfFlight.cc.

[11] `ClusterCounting` module in DELPHES. URL: https://github.com/delphes/delphes/blob/master/modules/ClusterCounting.cc.

[12] T. A. collaboration. CERN-LHCC-2024-003 ; ALICE-TDR-021. 2024. URL: https://cds.cern.ch/record/2890181?ln=en.

[13] M. Lucchini et al. “New perspectives on segmented crystal calorimeters for future colliders”. In: *Journal of Instrumentation* 15.11 (Nov. 2020), P11005. DOI: 10.1088/1748-0221/15/11/P11005.

[14] A. D. Vecchio et al. “Measurement of Higgs boson hadronic decays with $Z(\to \nu\nu/\ell\ell)H$ events at FCC-ee at $\sqrt{s} = 240$ GeV”. In: *CDS* (2023). DOI: 10.17181/rxdmc-4sa60.

[15] G. Salam, G. Soyez, and M. Cacciari. *Guidance through FastJet / jet algorithms for FCC-ee*. Presented at the FCC Physics Performance Meeting. June 2022. URL: https://indico.cern.ch/event/1173562/contributions/4929025/attachments/2470068/4237859/2022-06-FCC-jets.pdf.

[16] S. Di Vita et al. “A global view on the Higgs self-coupling at lepton colliders”. In: *Journal of High Energy Physics* 2018.2 (Feb. 2018). ISSN: 1029-8479. DOI: 10.1007/jhep02(2018)178. URL: http://dx.doi.org/10.1007/JHEP02(2018)178.

[17] B. Grzadkowski et al. “Dimension-Six Terms in the Standard Model Lagrangian”. In: *JHEP* 10 (2010), p. 085. DOI: 10.1007/JHEP10(2010)085. arXiv: 1008.4884 [hep-ph].

[18] K. Asteriadis et al. *Prospects for New Discoveries Through Precision Measurements at e^+e^- Colliders*. 2024. arXiv: 2406.03557 [hep-ph]. URL: https://arxiv.org/abs/2406.03557.

[19] K. Asteriadis et al. *The $e^+e^- \to ZH$ Process in the SMEFT Beyond Leading Order*. 2024. arXiv: 2409.11466 [hep-ph]. URL: https://arxiv.org/abs/2409.11466.

[20] A. Mehta and N. Rompotis. *$H \to$ invisible at FCC-ee*. Presented at the sixth FCC Physics Workshop, Krakow, Poland. Jan. 2023. URL: https://indico.cern.ch/event/1176398/contributions/5208291/attachments/2580000/4449733/mehta%20(2).pdf.

[21] M. Moretti, T. Ohl, and J. Reuter. “O’Mega: An Optimizing matrix element generator”. In: *Proceedings, Physics and Experimentation at a Linear Electron-Positron Collider, 2nd ECFA/DESY Study*. Feb. 2001, pp. 1981–2009. arXiv: hep-ph/0102195.

[22] T. Sjöstrand, S. Mrenna, and P. Skands. “PYTHIA 6.4 physics and manual”. In: *JHEP* 05 (2006), p. 026. DOI: 10.1088/1126-6708/2006/05/026. arXiv: hep-ph/0603175.

[23] URL: https://github.com/HEP-FCC/FCC-config.

[24] Particle Data Group, P. Zyla, et al. "Review of Particle Physics". In: *Prog. Theor. Exp. Phys.* 2020.8 (2020), p. 083C01. DOI: 10.1093/ptep/ptaa104.

[25] C. Bierlich et al. "A comprehensive guide to the physics and usage of PYTHIA 8.3". In: *SciPost Phys. Codeb.* 2022 (2022), p. 8. DOI: 10.21468/SciPostPhysCodeb.8. arXiv: 2203.11601 [hep-ph].

[26] S. Agostinelli et al. "GEANT4 – a simulation toolkit". In: *Nucl. Instrum. Meth. A* 506 (2003), p. 250. DOI: 10.1016/S0168-9002(03)01368-8.

[27] M. Frank et al. "DD4hep: A Detector Description Toolkit for High Energy Physics Experiments". In: *J. Phys. Conf. Ser.* 513 (2014). Ed. by D. L. Groep and D. Bonacorsi, p. 022010. DOI: 10.1088/1742-6596/513/2/022010.

[28] M. A. Thomson. "Particle Flow Calorimetry and the PandoraPFA Algorithm". In: *Nucl. Instrum. Meth. A* 611 (2009), pp. 25–40. DOI: 10.1016/j.nima.2009.09.009. arXiv: 0907.3577 [physics.ins-det].

[29] `CLDConfig` repository. URL: https://github.com/key4hep/CLDConfig.

[30] A. Sailer et al. "The Key4hep software stack: Beyond Future Higgs factories". In: *21th International Workshop on Advanced Computing and Analysis Techniques in Physics Research: AI meets Reality*. Dec. 2023. arXiv: 2312.08151 [hep-ex].

[31] A. Hoecker et al. *TMVA - Toolkit for Multivariate Data Analysis*. 2009. arXiv: physics/0703039 [physics.data-an].

This paper has been typeset from a TEX / LATEX file prepared by the author.